Research Article | Vol. 11, No. 11 / 1 November 2020 / Biomedical Optics Express 6197
Biomedical Optics EXPRESS

# Imaging of PD-L1 in single cancer cells by SERS-based hyperspectral analysis

WEI ZHANG,[1] JAKE S. RHODES,[2] KEVIN R. MOON,[2] BEATRICE S. KNUDSEN,[3] LINDA NOKOLOVA,[4] AND ANHONG ZHOU[1,*]

[1]Department of Biological Engineering, Utah State University, Logan, UT 84322, USA
[2]Department of Mathematics and Statistics, Utah State University, Logan, UT 84322, USA
[3]Department of Pathology University of Utah, Salt Lake City, UT 84112, USA
[4]Electron Microscopy Core Laboratory, University of Utah, Salt Lake City, UT 84112, USA
*Anhong.Zhou@usu.edu

**Abstract:** We developed a hyperspectral imaging tool based on surface-enhanced Raman spectroscopy (SERS) probes to determine the expression level and visualize the distribution of PD-L1 in individual cells. Electron-microscopic analysis of PD-L1 antibody - gold nanorod conjugates demonstrated binding the cell surface and internalization into endosomal vesicles. Stimulation of cells with IFN-γ or metformin was used to confirm the ability of SERS probes to report treatment-induced changes. The multivariate curve resolution-alternating least squares (MCR-ALS) analysis of spectra provided a greater signal-noise ratio than single peak mapping. However, single peak mapping allowed a systematic subtraction of background and the removal of non-specific binding and endocytic SERS signals. The mean or maximum peak height in the cell or the mean peak height in the area of specific PD-L1 positive pixels was used to estimate the PD-L1 expression levels in single cells. The PD-L1 levels were significantly up-regulated by IFN-γ and inhibited by metformin in human lung cancer cells from the A549 cell line. In conclusion, the method of analyzing hyperspectral SERS imaging data together with systematic and comprehensive removal of non-specific signals allows SERS imaging to be a quantitative tool in the detection of the cancer biomarker, PD-L1.



## 1. Introduction

The Programmed death ligand 1 (PD-L1) / programmed death 1 (PD-1) ligand – receptor system forms an immune checkpoint between activated immune cells to dampen the immune response, preventing tissue destruction and autoimmunity [1,2]. PD-L1 is expressed on the surface of multiple cell types, including cancer cells and macrophages [2], while PD-1 is expressed on cytotoxic, $CD8^+$ T-cells. Cancer cells hijack PD-L1 over-expression as a mechanism of immune evasion [2,3]. Recently, immune checkpoint inhibitors (e.g. nivolumab and pembrolizumab, both approved by the FDA [3]), blocking PD-L1/PD-1 interactions have gained momentum as novel anticancer therapeutics. These drugs achieve durable cancer control in several malignancies including metastatic lung cancer and melanoma [4].

The measurement of PD-L1 expression by immunohistochemistry is used as a companion diagnostic to identify patients who might respond to immune checkpoint inhibition [5]. PD-L1 expression is regulated by multiple cytokines, most notably gamma-interferon (IFN-γ), and through STAT and NF-κB pathway activation [6] as well as by metformin via glycosylation [7]. PD-L1 expression differs across cancers, despite exposure to the same growth factor milieu of the fetal calf serum, suggesting cell intrinsic regulation of PD-L1 expression. For example, the human lung adenocarcinoma cell line, A549, expresses low PD-L1 [8], while the human breast cancer cell line, MDA-MB-231, expresses high PD-L1 levels [9].

Raman microspectroscopy (RM) is non-destructive and measures vibration and rotational modes of macromolecules at the single-cell level using inelastic laser light scattering [10]. Surface

#401142 https://doi.org/10.1364/BOE.401142
Journal © 2020 Received 26 Jun 2020; revised 23 Sep 2020; accepted 24 Sep 2020; published 8 Oct 2020

Biomedical Optics EXPRESS

enhanced Raman spectroscopy (SERS) enhances the Raman signals by molecules absorbed on rough metal surfaces and has rapidly progressed from a bench-scale spectroscopic tool to a preclinical diagnosis technique [11]. Recently, our lab developed multiplexed SERS probes to visualize the distribution of G-coupled protein receptor 120 (GPR-120) and the clustering of differentiation receptor 36 (CD36) on taste bud cells [12]. Compared to other imaging systems, SERS imaging offers high sensitivity and specificity at a single cell level without the limitations caused by tissue autofluorescence and photobleaching. On the other hand, the cell-based SERS experiments generally can be divided into two methodologies: the SERS-reporter (SERS-label) approach or the reporter-free (label-free) SERS approach [13]. The nanoparticles either labeled with a Raman reporter molecule [14–16] or label-free [17–19] might be internalized by cells, which can contribute to the background signals but is often ignored. PD-L1 distribution on MDA-MB-231 cells has been visualized at an intensity of 1580cm$^{-1}$ of the Raman reporter *p*-mercaptobenzoic acid (*p*-MBA) after background subtraction [20]. However, this approach discarded most of the spectral information and only used a single Raman peak. This limitation can be overcome by multivariate spectral analysis methods, such as the multivariate curve resolution-alternating least squares (MCR-ALS).

MCR-ALS is a powerful approach that is commonly used to identify complex spectral profiles and visualize the distribution of major components that are spectrally different in cell or tissue samples [21–23]. The combination of SERS and MCR-ALS has been successfully applied to quantifying nitroxoline [24] and adenosine [25] in clinical samples. However, MCR-ALS may not be the method of choice for Raman spectra that contain a single, dominant peak. When dealing with antibody – SERS conjugates for detection of proteins in cells, the nonspecific binding of the SERS particles as well as of the antibody has to be subtracted to arrive at specific binding intensities. However, specific binding measurements are rarely reported when using antibody – SERS probes. When the assay's goal is to guide treatment decision, such as in the case of PD-L1 expression levels, separating specific from non-specific signals is critical.

In this paper, we analyze the PD-L1 signal obtained from SERS by MCR-ALS and single peak quantification within segmented cell boundaries. This approach generates a high-resolution, spatial map of PD-L1 expression on the surface of single cancer cells. The SERS probes are conjugated to PD-L1, allowing specific binding to the target molecule on the cell surface. Even without antibody, nanoparticles can non-specifically adhere to the cell surface (extracellular) and can be endocytosed by the cells (intracellular), which can also contribute the background signals in Raman measurements. These conditions complicate the interpretation of the data and have been overlooked in most SERS detection applications [26,27]. Included in the workflow are baseline subtraction and background processes, which remove non-specific binding and endocytic SERS intensities. Since expression of PD-L1 is known to be regulated by IFN-γ or metformin, we question whether SERS can detect expression changes in PD-L1 after drug treatment.

## 2. Materials and methods

### 2.1. Cell culture

A549 cells and MDA-MB-231 cells were purchased from ATCC (Manassas, VA, USA) and cultured in F-12 k medium containing 10% fetal bovine serum (Thermo Fisher Scientific, Waltham, MA, USA) and a 1:1 mixture of Dulbecco's-modified eagle's medium (DMEM) supplemented with 5% fetal bovine serum, respectively. HEK293 cells were generously donated from Dr. Timothy Gilbertson in University of Central Florida and cultured in DMEM-GlutaMAX media (Life Technologies, 10569-010), supplemented with 10% Tet-free fetal bovine serum (Fisher, NC0290780), Blasticidin S HCl (10 µg/mL) and Hygromycin B (100 µg/mL). All cell lines were cultivated with 5% at 37 °C $CO_2$ in a humidified atmosphere. Metformin was purchased from Sigma-Aldrich (D150959, St. Louis, USA).

Biomedical Optics EXPRESS

### 2.2. Nanoparticle conjugation and characterization

5, 5-dithiobis(2-nitrobenzoic acid) (DTNB) anti-PD-L1 antibody conjugated nanoprobes were synthesized for Raman SERS detection (Fig. S1). Briefly, 1 ml (39 μg/ml) Au nanorods (A12-10-780-CTAB, Nanopartz Inc. Loveland CO, USA) with 10 nm in diameter and 40 nm in length (polydispersity index = 7~8%) was first sonicated with 10 μL DTNB (1 mM, Sigma-Aldrich, St. Louis, MO) for 30 min. Then 10 μL HOOC- Polyethylene glycol (PEG)-SH (1 mg/ml, MW 5000, Nanocs Inc. USA) was added to conjugate with nanorods for 15 min, followed by 40 μL PEG-SH (1 mg/ml, MW5000, Nanocs Inc. USA) sonication for another 30 min. After centrifuging for 15 min (12000g) to remove excess DTNB and PEG, particles were resuspended in 500 μL DI water and mixed with freshly prepared ethyl(dimethylaminopropyl) carbodiimide (EDC) (10 mM, 10 μL, Sigma-Aldrich, St. Louis, MO) and N-Hydroxysuccinimide (NHS) (25 mM, 10 μL, Sigma-Aldrich, St. Louis, MO) solution. After a 30-minute reaction, the excess supernatant was removed after centrifugation (12000g, 15 min). The resultant particles were resuspended in 200 μL PBS and conjugated with PD-L1 antibody (0.2 mg/mL, 10 μL, Acris, Herford, Germany) for another 1 h. Finally, particles were resuspended in 100 μL Phosphate-buffered saline (PBS) after discarding excessive antibody. The functionalized nanoparticles (estimated as 19.5 μg/ml) can be preserved for several days at 4 °C. The SERS probes incubated with live cells for 24 hours. Cells were either imaged life using Raman spectroscopy, or fixed and imaged via transmission electron microscope JEOL-JEM 1400 Plus at 120 kV, at Electron Microscopy Core Laboratory in University of Utah. Cells were seeded on ACLAR discs and grown as monolayer culture until reaching the desired confluency and incubated with SERS probes for 24 h. After washing with PBS for three times, the cells were fixed with 1% paraformaldehyde and 2.5% glutaraldehyde in 0.1M Cacodylate buffer and incubated at 4°C for overnight. Next day, the specimens were rinsed twice in cacodylate buffer and postfixed in 2% osmium tetroxyde for 1 hr at room temperature, followed by rinse with the same buffer and $dH_2O$. The specimens were poststained with uranyl acetate for 1 hr at room temperature followed by dehydration with graded ethanol series (50, 70, 95, 100%) and absolute acetone for 10 min each step. The ACLAR disks with the cells were infiltrated with epoxy resin EMBED -812, embedded and polymerized at 60°C for 48hrs. Thin sections (70 nm) were obtained using Leica UC6 Ultratome (Leica Mycrosystems, Vienna, Austria) poststained with uranyl acetate and lead citrate and imaged with electron transmission microscope JEOL-JEM 1400 Plus at 120 kV. All reagents used in TEM imaging were from Electron Microscopy Sciences, PA, USA.

### 2.3. Raman spectroscopy

The Raman spectra were measured by a Renishaw inVia Raman spectrometer (controlled by WiRE 3.4 software, Renishaw, UK) connected to a Leica microscope (Leica DMLM, Leica Microsystems, Buffalo Grove, IL, USA), equipped with a 785 nm near-IR laser that was focused through a 63 × NA = 0.90 water immersion objective (Leica Microsystems, USA). The laser intensity before and after travelling through the 63× objective was 110 mW and 29.4 mW, respectively (measured with LaserCheck, Coherent Inc., Portland, OR, USA). The standard calibration peak for the spectrometer with silicon mode at a static spectrum was $520.5 \pm 0.1\ cm^{-1}$. Cells were cultured on $MgF_2$ (United Crystals Co., Port Washington, NY, USA) for 24 h and incubated with either IFN-γ (0, 10 and 100 ng/ml) or metformin (0, 6 mM) for 24 h. SERS probes were added into the cell culture system 24 hours prior to streamline mapping (100% power, 5s exposure time, 0.8 μm step). Cell were washed three times by PBS before Raman measurements. A rectangle area covering the whole single cell was selected to collect the spectra. Image segmentation was used to exclude the spectra collected on the background outside of the cell area. The remaining spectra in each measurement were baseline corrected using asymmetric least-squares smoothing in OriginLab 2020 (asymmetric factor: 0.001, threshold: 0.05, smoothing factor: 5, number of iterations: 10). MCR-ALS was used to analyze the

Biomedical Optics EXPRESS

hyperspectral imaging data. The threshold level in the SERS image was defined based on the results in the negative control experiment using gold nanorod + DTNB without conjugating antibody (thus no recognition binding with PD-L1 receptor). The 99$^{th}$ percentile of SERS intensity counts (peak height) from each cell was used to calculate the average peak height across all cells in the control group. This average was used as the threshold to separate specific and non-specific intensity counts in each pixel (Fig. S2). A paired *t*-test was used to compare the mean difference between the control and various treatments groups. We also determined the percentage of PD-L1 positive area over the whole cell area after removing the non-specific binding signals. Pearson correlation analysis was used to characterize the relationship between the percentage and mean intensity of PD-L1 positive area in each treatment. $P<0.05$ was considered significant. Analysis was performed in OriginLab 2020 (Massachusetts, USA) and in MATLAB 2019b. All data are represented as mean ± sd.

### 2.4. MCR-ALS

MCR is designed to decompose the spectral profiles and concentration levels of a multi-component (chemical) compound. MCR-ALS analysis is an iterative approach to MCR based on alternating least squares matrix factorization. The algorithm factors an $n\times d$ matrix, $D$, ($n$ being the number of collected samples, and $d$ the number of features, in this case, wavenumbers) into two matrices $C$ (an $n\times k$ matrix of concentrations) and $S^T$ (a $k\times d$ matrix of spectrum profiles). Here, $k$ is the number of components of the compound, as determined by either prior knowledge or given by an estimation, typically done using PCA (principal components analysis), or singular value decomposition (SVD). The factorization takes the form below, where $E$ is an error term.

$$D = CS^T + E$$

The idea behind the alternating least squares method is to minimize the error of the factorization problem. The error estimation is calculated between the data matrix and the estimated factors and the optimization problem (ALS) is solved iteratively. That is, after fixing, $C$, minimize $\|\hat{D}_{PCA} - \hat{C}\hat{S}^T\|^2$ over $S^T$. Then $S^T$ is fixed and $\|\hat{D}_{PCA} - \hat{C}\hat{S}^T\|^2$ is minimized over $C$. At each iteration, the lack of fit is calculated using

$$LoF = 100\sqrt{\frac{\sum_{ij} e_{ij}^2}{\sum_{ij} d_{ij}^2}}$$

where $d_{ij}$ is an element of either the original data matrix D, or the principal component analysis (PCA) scores of D ($\hat{D}_{PCA}$), and $e_{ij}$ is the corresponding residual given by the difference of the matrix D (or $\hat{D}_{PCA}$), and the MCR-ALS construction [28]. The process is repeated until a convergence criterion is met [28].

The optimization problem has additional optional constraints, such as non-negativity (of either the concentration, spectral profile, or both), unimodality, and closure [28,29]. Due to the nature of the Raman spectra, we activate the non-negativity constraint (to ensure wavenumber measurements are non-negative). Unimodality of concentration was often exhibited without enforcing the constraint.

The implementation we used was in MATLAB (2019b). Slight adaptations were made to the original package to allow for automation over multiple image samples.

The estimation of component $i$ of the original matrix $D$, denoted $D_i$, may be recovered by taking the outer product of the $i^{th}$ column of $C$ by the $i^{th}$ row of $S^T$, that is, $D_i = C_{.i}S_{i.}^T$ The summation of all of the components (plus the error) reconstructs the original matrix $D$, that is, $D = \sum_i D_i + E$.

Biomedical Optics EXPRESS

### 2.5. Imaging segmentation detection

Prior to the application of image segmentation, the light cell image was cropped to the exact dimensions as the spectral image to align the areas where the cell is present to the Raman spectra captured. Edge detection was performed in MATLB 2019b using the Image Processing Toolbox. The bitmap light cell image undergoes a series of alterations prior to the final result. Imaging segmentation makes use of the gradient-magnitude of the colors within the image to identify boundaries of objects within an image [30]. After this preliminary step, the edges are dilated (broadened) to fully encapsulate the interior of the cell within the image. Once the edges are sufficiently dilated to enclose the cell, the cellular image is filled to fully segment the cellular presence and absence. The cellular edges are then smoothed to improve the image representation. Once the cell is identified within the image, coordinates where the cell is present are mapped to the original coordinate system produced during Raman imaging for further spectral analysis.

## 3. Results

The end-to-end pipeline of the hyperspectral image analysis is shown in Fig. 1. The approach allows data collection from single cells to determine the distribution of PD-L1 within subdomains of the cell membrane. First, cells were labeled with anti-PD-L1 antibody conjugated to surface enhanced Raman scattering (SERS) nanoparticles. Second, the binding of the antibody to PD-L1 on the cell surface was visualized using Raman spectroscopy (single peak mapping or MCR-ALS). In addition, a brightfield image was used to delineate the boundary of the cell. Raman spectra inside the segmented cell area were retained. The background was subtracted to reveal the peak height of Raman signals. The mean and maximum intensities of PD-L1 expression were determined over the entire cell. Alternatively, a threshold was established based on non-specific binding, to distinguish PD-L1 positive from PD-L1 negative pixels. Thereafter, the percentage of PD-L1 positive cell area inside the cell outline and mean intensity within the PD-L1 positive area were determined.

### 3.1. Cell labeling with PD-L1-SERS nanoparticles (PD-L1 probe)

To determine the binding characteristics of the functionalized PD-L1 probe, the probe was incubated with A549 cells for 24 h at 37°C and imaged by TEM (Fig. 2). The size of the rod-shaped nanoparticle (width $14.172 \pm 0.598$ nm and length $45.377 \pm 2.995$ nm, Fig. 2(B) inlet) after multiple conjugation steps, is roughly equal to the original dimension (10 nm diameter and 40 nm length) provided by the manufacturer. TEM showed many PD-L1 probes on the cell surface, consistent with the subcellular location of the PD-L1 receptor (Fig. 2(A)-(B)). In addition, several probes entered the cell and were surrounded by membrane-bound structures, indicating that PD-L1 probes are internalized by endocytosis (Fig. 2(C)-(D)). Notably, the probe maintained its structural integrity outside and inside the cell. After endocytosis, nanoparticles were shown to aggregate within vesicular structures [31,32] from which they can be released into the cytoplasm [33]. After incubation with cells for 24 h, probes were densely aggregated within membrane-bound vesicular structures (denoted as "V" in Fig. 2(D)). No PD-L1 probes were observed inside the nucleus (denoted as "N" in Fig. 2(C)-(D)) or within mitochondria (denoted as "M" in Fig. 2(D)), which is similar to previously reported findings [31,32]. According to the recent reports, the SERS signals from endocytic nanoparticles were decreased to comparable level of the signals from the cellular components [14,15]. In our study, all the cellular intrinsic peaks (~1000 counts) were overwhelmed by enhanced Raman signals (~8000 counts) from cell surface (Fig S1B). Therefore, the endocytosed nanorods labeled with DTNB may not contribute in a significant way to the overall specific signal in spectral data. In order to address the issue raised from non-specific binding (nanorod labeled with or without DTNB) and endocytosed nanorods, we seek to apply the following methods to remove the potential background signal.

Biomedical Optics EXPRESS

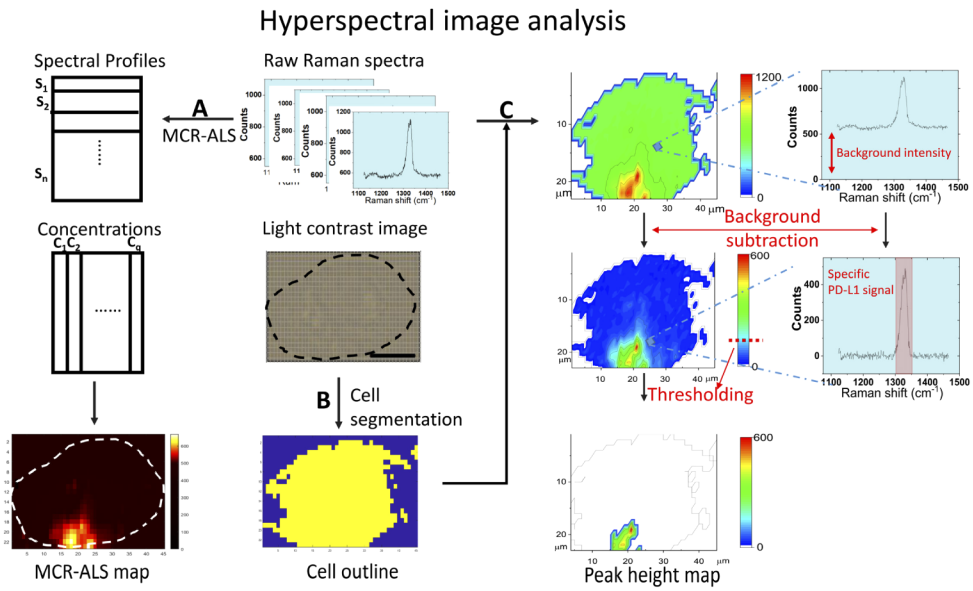


**Fig. 1.** Schematic illustration of our data processing approach. Raman spectra are collected throughout the whole slide and analyzed by MCR-ALS (A). In addition, cells are imaged using a brightfield microscope and the image is processed for cell segmentation (B). Raman spectra are extracted from the inside of the segmented region and the maximum peak height of each spectrum is recorded (C). The background is subtracted from the maximum peak height to obtain the Raman intensity signal. Intensity measurements are displayed as a heatmap over the cell and a threshold reflecting the non-specific binding is used to distinguish positive and negative pixels. The approach enables calculations of average signal intensity in the whole cell as well as in the area encompassed by positive pixels.

### *3.2. Visualization of PD-L1 on the surface of single cells*

Three cell lines, MDA-MB-231 (breast cancer), A549 (lung cancer), and HEK293 cells (human embryonic kidney cell) were treated either with control, unconjugated nanorods containing the Raman reporter, DTNB (no PD-L1 antibody), or with DTNB-nanorods conjugated with the PD-L1 antibody. The MDA-MB-231 and A549 cells are PD-L1 positive, while HEK293 cells do not express PD-L1 and were used as a control cell line to evaluate the non-specific binding of the PD-L1 antibody. A spectrum was collected from every pixel within a rectangular area covering the entire cell (Fig. 3 upper panel). Because the spectral characteristics of the DTNB probe revealed a single, dominant peak at 1328cm$^{-1}$, we compared the intensity maps from the MCR-ALS multivariate analysis method to the single peak height analysis. To remove the background signal, we extracted spectra from an area with a low peak height (green circle) and subtracted the background from all spectra of the cell. The raw and corrected (background removed) spectra from control group and PD-L1 probe treated group of A549 cell was shown in Fig S2. The MCR-ALS analysis resulted in a better signal-to-noise ratio and less noise compared to the single peak height method (Fig. 3, middle and bottom panels) demonstrating the advantage of multivariate analysis over univariate approaches. Compared to PD-L1 negative HEK293 cells, a strong signal was observed in MDA-MB-231 cells and A549 cells. Results in the control cells incubated with unconjugated DTNB-nanorods did not demonstrate a difference in signal intensity across the three cell lines. Together, these findings are consistent with the known expression of PD-L1 in breast and lung cancer cells but not in HEK293 cells. However, the results also demonstrate that background and non-specific binding cause significant technical and

Biomedical Optics EXPRESS

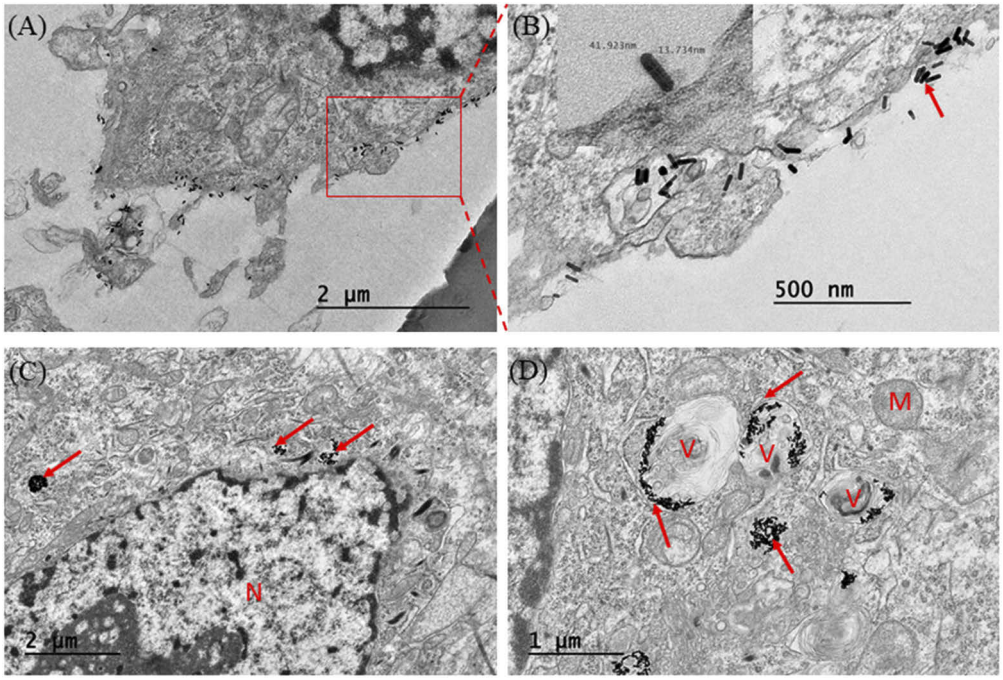


**Fig. 2.** Transmission Electron micrographs of A549 cells incubated with the PD-L1 probe for 24 h. The nanoparticles appear as electron dense rod-shaped structures. (A): Surface binding of the SERS probe, the probe is seen on the cell membrane; (B): Enlarged area noted by red square in (A) and the size of a representative single nanorod is shown in inlet; (C-D): Endocytic uptake of SERS probes into cells, formation of SERS aggregates (red arrow) within endosomal vesicles (V). SERS probes are not observed inside the nucleus (N) or within mitochondria (M).

biological errors in the quantitative assessment of PD-L1 expression. Therefore, we proceeded to systematically evaluate these sources of error and to remove them in order to generate specific binding maps for the PD-L1 antibody in individual cells.

To establish the threshold above which we detect specific binding of the PD-L1 antibody, we determined the intensity levels in control groups, which are generated by the DTNB nanorod alone (Fig. 4(A)). The averaged 99$^{th}$ percentile in the distribution of peak heights was used as the threshold to separate positive from negative PD-L1 pixels. The threshold was applied across all cells labeled with the PD-L1 antibody in the same experiment. The thresholds are 255.99 Raman counts for MDA-MB-231 cells, and 318.79 Raman counts for A549 cells (See details in Fig. S3.). Most individual cells incubated with PD-L1 probes revealed high magnitude signals and the average signal in A549 lung cancer cells and MDA-MB-231 breast cancer cells was significantly greater than the antibody-free control signal. In addition, the average signal in MDA-MB-231 cells was greater than the average signal in A549 cells, but the difference did not reach statistical significance. Interestingly, we observed a biphasic distribution of signals in A549 cells, with a number of cells expressing low/no PD-L1. No significant difference was seen between negative control and the PD-L1 probe in HEK293 cell (Fig. 4(A), purple box), indicating that PD-L1 antibody has no contribution in non-specific binding.

In single cell Raman imaging, the Raman scanning area covers all of the cell and additional extracellular area (Fig. 4(B)). Raman spectra within the cell area were retained and further background corrected, while Raman spectra outside the cell boundary were dismissed. Figure 4(C)

Biomedical Optics EXPRESS

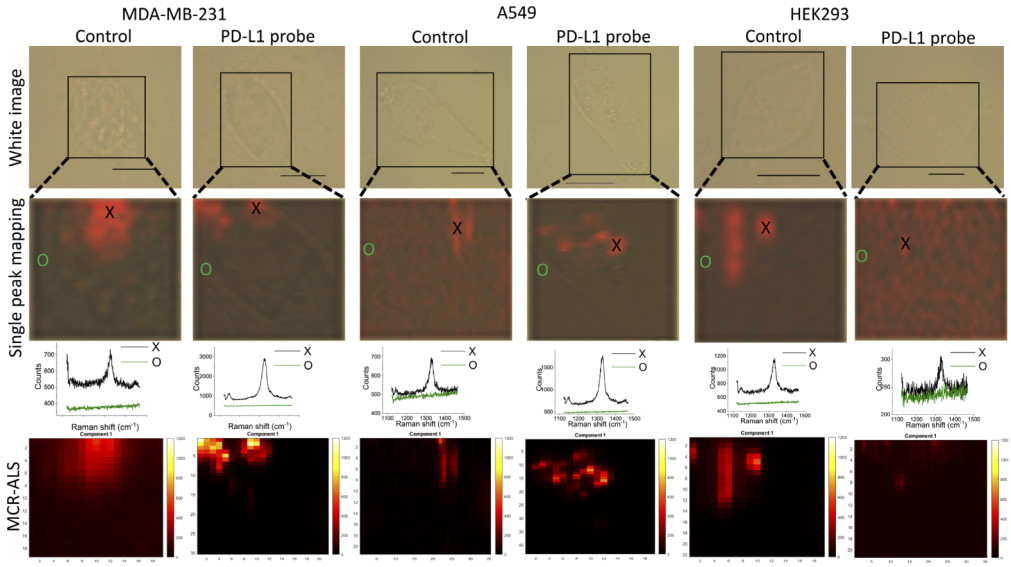


**Fig. 3.** Comparison of single peak mapping and MCR-ALS mapping in three cell lines, MDA-MB-231, A549, HEK293 after incubation with gold nanorods + DTNB (negative control) and PD-L1 probes. Light images of single cells are shown in the first row and the area used to collect Raman spectra is shown by the black rectangle. The results from the single peak ($1328 cm^{-1}$) mapping are shown in the second row. The third row depicts spectra recorded from the pixel area designated as X (black line) and O (green line). In the fourth row, MCR-ALS mapping results are shown, using the same color bar range from 0-1200 counts (fourth row). Scale bar: 10 µm.

illustrates a heatmap of background corrected SERS peaks within the outline of a representative A549 cell. A cluster of pixels with high intensity signals is surrounded by a large region of pixels at or below the non-specific binding threshold. After subtracting the threshold of non-specific signal indicated in Fig. 4(A), the final heatmap is generated in Fig. 4(D), only showing colors for specific PD-L1 positive pixels within the cell.

### 3.3. *Effect of IFN-γ on PD-L1 expression*

Treatment of cells with IFN-γ at a concentration of 0-100 ng/ml was used to induce PD-L1 expression [34]. For quantitative analysis of PD-L1, we analyzed Raman peaks at $1328 cm^{-1}$ and calculated 1) the mean peak height within the cell outline, 2) the maximum peak height within the cell, and 3) the mean peak height in the area encompassed positive pixels (illustrated in Fig. 4(D)). In addition, we determined the percentage of the cell area that contains PD-L1 positive pixels.

First, we used the mean peak height inside cells to represent the average PD-L1 expression level. This approach did not reveal significant changes in PD-L1 expression levels before and after treatment with IFN-γ ($p>0.05$ Fig. 5(A)) for both A549 and MDA-MB-231 cells. Next, we used the maximum peak height and observed a significant increase in PD-L1 in A549 cells, but not in MDA-MB-231 cells (Fig. 5(B)). In addition, the maximum peak height increases proportional to the amount of IFN-γ used for stimulation. Finally, we analyzed the mean peak height within the area of PD-L1 positive pixels (illustrated in Fig. 4(D)). While we observed a significant increase after IFN-γ treatment (Fig. 5(C)), the difference before and after treatment was less pronounced than that in Fig. 5(B). Altogether, the results demonstrate that the stimulation of A549 cells with IFN-γ causes a significant increase in PD-L1 expression.

Biomedical Optics EXPRESS

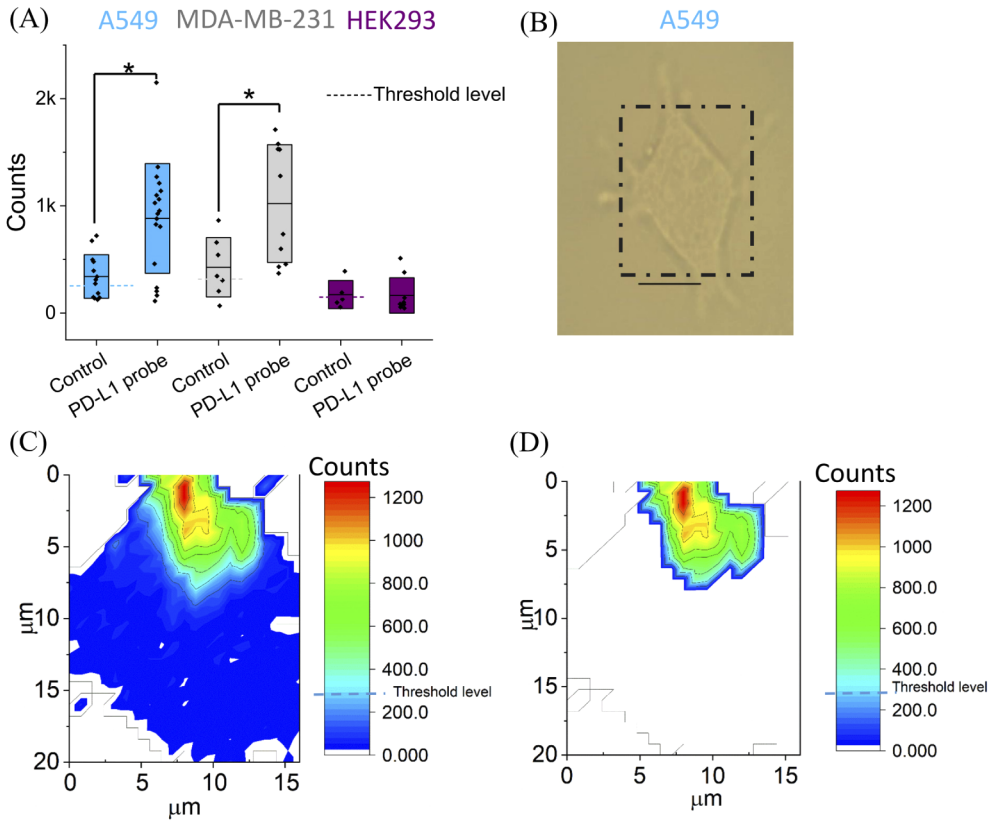


**Fig. 4.** Workflow to generate a mask of specific maximum peak intensities from SERS signals. A549 and MDA-MB-231 cells were used as positive controls and HEK293 cells as a negative control of PD-L1 expression. At least 7 individual cells from each cell line incubated with DTNB-nanorod or nanorod – PD-L1 antibody conjugates were imaged (A). 99$^{th}$ percentile of SERS intensities in the control group (dashed lines) was used as the threshold to separate positive from negative pixels and averaged to calculate the noise level (dash line). The scanning area covering the whole single cell (A549 cell with only PD-L1 probe as an example) is denoted by the black dash rectangle in (B). The image was further segmented to obtain the outline of the cell. Raman spectra inside the cell were retained as shown in (C). The heatmap of PD-L1 SERS signals after thresholding to separate specific (color) and non-specific (white) signals is shown in (D). *p<0.05 from paired *t*-test. Scale bar in (B): 10 μm.

Biomedical Optics EXPRESS

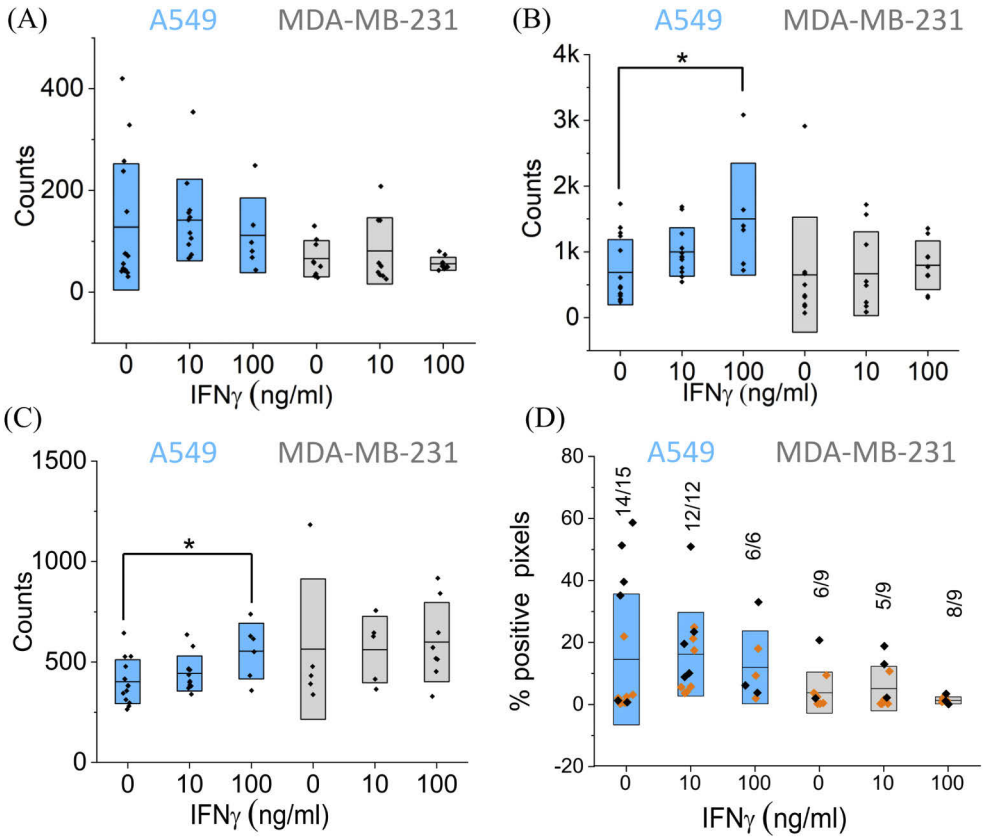


**Fig. 5.** IFN-γ (0, 10, 100 ng/ml) stimulation of A549 and MDA-MB-231 cells. PD-L1 expression measured by averaged SERS intensity counts (A), maximum SERS intensity counts (B) or SERS intensity counts averaged within the PD-L1 positive pixel area (C). The percentage of PD-L1 positive area within the cell outline is shown in (D). Numbers above each box indicate the number of cells positive for PD-L1 divided by the total cell number cells analyzed. Cells are divided into two groups, separated by the mean signal intensity of PD-L1 positive pixels. Black squares mark cells with above the mean intensities and orange squares cells with below the mean intensities. The mean of the % positive pixel area is shown by the black line across the box. A paired t-test was performed to determine the significance of difference between control and treatment groups. * $p<0.05$; N = 6-12 cells.

Biomedical Optics EXPRESS

So far, measurements do not take into consideration whether PD-L1 expression is localized to a specific region or spread throughout the cell. To determine the extent of localized PD-L1 expression, we calculated the percentage of PD-L1 positive pixels (illustrated in Fig. 4(D)), inside the cell boundary. Representative cells with low, medium and high percentages of PD-L1 positive areas are shown in Fig. S4-5. The percentage of PD-L1 positive pixels is shown in Fig. 5(D). To visualize the relationship between PD-L1 positive pixels and PD-L1 expression levels, we colored cells with high average PD-L1 expression in black and cells with low average PD-L1 expression in yellow. No significant correlation was observed between %PD-L1 positive area and PD-L1 expression level (Table S1).

### 3.4. Effect of metformin on PD-L1 expression

Since we observed IFN-γ regulation of PD-L1 only in A549, but not in MDA-MB-231 cells, we treated only A549 cells with metformin. Measurement of PD-L1 expression using antibody-SERS conjugates revealed a significant decline of PD-L1 after treatment (Fig. 6(A)-(C)). Furthermore, the decrease in expression was observed in all image processing methods (cell average, peak height, positive pixel average). In addition, the percentage of PD-L1 positive pixels was significantly reduced after metformin treatment (Fig. 6(D)). Together these data confirm that metformin down-regulates PD-L1 expression.

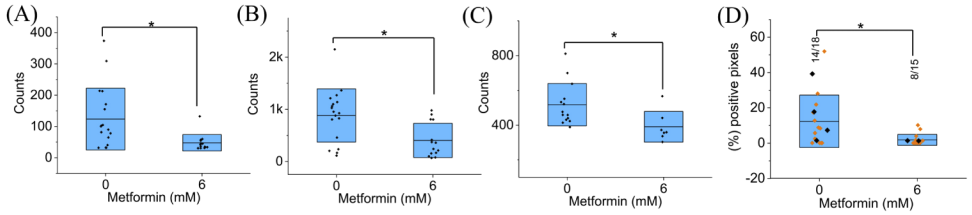


**Fig. 6.** Metformin treatment reduces PD-L1 expression. A549 lung cancer cells were treated with 6 mM metformin. Data were collected as described in Fig. 5. The average peak height measured in counts is shown in (A), maximum peak heights are shown in (B) and average peak height in the positive pixel area (illustrated in Fig. 4(D)) is shown in (C). The numbers above each box indicate PD-L1 positive over total cells analyzed. In D, cells are divided into an above the mean intensity (black squares) and a below the mean intensity group (orange squares). A paired t-test was performed to determine the significance of difference between control and treatment groups. * $p<0.05$; N=15-18 cells.

## 4. Discussion

Traditionally, expression levels of cell surface receptors are measured by enzyme-linked immunosorbent assay (ELISA) or flow cytometry of detached, rounded cells. These methods are ideally suited to generate data from cell populations but cannot capture the subcellular location of receptor expression. The spatial resolution needed for subcellular analysis of cell cultures can be provided by fluorescent probes or by Raman active probes. The probes are conjugated to antibodies that bind to the target protein of interest. However, antibodies and probes generate non-specific signals that need to be eliminated to determine true protein expression levels.

In this study, we demonstrate that PD-L1 expression in cancer cells (MDA-MB-231 and A549 cell) can be measured with high spatial resolution using SERS. To obtain highly specific SERS signals, we subtracted the background, which consists of the baseline of the spectrum next to the peak at 1328cm$^{-1}$. In addition, we removed nonspecific binding signals by setting a threshold to distinguish positive and negative signals. Applying both, background and non-specific binding corrections, we obtained specific and high-quality data for PD-L1 antibody binding. Furthermore,

Biomedical Optics EXPRESS

we used three methods to process the hyperspectral imaging data: whole cell peak height average, peak height maximum and peak height average amongst positive pixels. Obtaining data from the three methods provides a deeper understanding of the spatial organization of SERS signals and PD-L1 expression in cancer cells [35].

Our study also shows that PD-L1 expression is stimulated by IFN-γ and inhibited by metformin in lung cancer cells (Fig. 5–6), which is consistent with recent reports [36–38]. In contrast, the treatment effect of IFN-γ in breast cancer cells was not significant, perhaps due to the inherently high expression level of PD-L1 in this cell line [9]. The single cell analysis by SERS mapping provides more information about the heterogeneity among individual cells in the cell line. Our results show that not all cells respond to IFN-γ or metformin (Fig. 5–6) and approximately 20% of cells were PD-L1 negative prior to treatment. Single-cell measurements allow us to recognize cell to cell differences, which cannot easily be noticed using conventional methods. The unique characteristics of SERS mapping generates data with high sensitivity and resolution. While this data demonstrates the heterogeneity of cells in the cancer cell lines, it also lets us appreciate limitations in interpreting single cell data. By comparing cell-to-cell variabilities with the variability of cell populations before and after treatment, we can gain insights into details of the treatment effect. Further studies with larger numbers of cell samples will be necessary to confirm the effects of IFN-γ and metformin on PD-1 expression in cancer cells.

This study demonstrates the successful application of Raman imaging with multivariate analysis and image processing methods on single cells. We successfully employed a multivariate method (MCR-ALS) on hyperspectral imaging data to visualize the distribution of PD-L1 in breast and lung cancer cells. We also used the height of the single, dominant peak in the Raman spectrum to estimate the expression levels of PD-L1. The latter approach has the advantage of allowing a systematic subtraction of non-specific binding and endocytic nanoparticles for each pixel in the cell outline. Whether background signals would be from intracellular or extracellular nanoparticles needs to be explored in the future. Image segmentation in brightfield images was performed to extract the spectra solely from within the cell area. Three methods of processing the data from the single peak heights of Raman spectra were compared. The average peak height in the PD-L1 positive pixel area appeared to be more reliable for hyperspectral imaging analysis than the average peak height across the entire cell. The results from this validation study of our newly fabricated PD-L1 specific SERS probes support further use of the probes for cell-based assays and as a tool for selection of cancer patients for treatment with PD-1/PD-L1 immune checkpoint inhibitors.

## Funding

ARUP Laboratories; University of Utah; Utah Agricultural Experiment Station; Graduate Research and Creative Opportunities (GRCO) from Utah State University.

## Acknowledgments

We would like to thank the support from Utah Agricultural Experiment Station and Graduate Research and Creative Opportunities (GRCO) funding of Utah State University. BSK thanks the University of Utah and ARUP Laboratories for supporting the project.

We thank the donation of HEK293 cell from Dr. Timothy Gilbertson (now from the University of Central Florida).

## Disclosures

The authors declare no conflicts of interest.

Biomedical Optics EXPRESS

See Supplement 1 for supporting content.

## References


1. A. Kythreotou, A. Siddique, F. A. Mauri, M. Bower, and D. J. Pinato, "Pd-L1," J. Clin. Pathol. **71**(3), 189–194 (2018).
2. Y. Wang, H. Wang, H. Yao, C. Li, J. Y. Fang, and J. Xu, "Regulation of PD-L1: Emerging Routes for Targeting Tumor Immune Evasion," Front. Pharmacol. **9**, 536 (2018).
3. J. Gong, A. Chehrazi-Raffle, S. Reddi, and R. Salgia, "Development of PD-1 and PD-L1 inhibitors as a form of cancer immunotherapy: a comprehensive review of registration trials and future considerations," Immunother. Cancer **6**(1), 8 (2018).
4. L. Zitvogel and G. Kroemer, "Targeting PD-1/PD-L1 interactions for cancer immunotherapy," OncoImmunology **1**(8), 1223–1225 (2012).
5. S. Heskamp, W. Hobo, J. D. Molkenboer-Kuenen, D. Olive, W. J. Oyen, H. Dolstra, and O. C. Boerman, "Noninvasive Imaging of Tumor PD-L1 Expression Using Radiolabeled Anti-PD-L1 Antibodies," Cancer Res. **75**(14), 2928–2936 (2015).
6. K. Abiko, N. Matsumura, J. Hamanishi, N. Horikawa, R. Murakami, K. Yamaguchi, Y. Yoshioka, T. Baba, I. Konishi, and M. Mandai, "IFN-gamma from lymphocytes induces PD-L1 expression and promotes progression of ovarian cancer," Br. J. Cancer **112**(9), 1501–1509 (2015).
7. J. H. Cha, W. H. Yang, W. Xia, Y. Wei, L. C. Chan, S. O. Lim, C. W. Li, T. Kim, S. S. Chang, H. H. Lee, J. L. Hsu, H. L. Wang, C. W. Kuo, W. C. Chang, S. Hadad, C. A. Purdie, A. M. McCoy, S. Cai, Y. Tu, J. K. Litton, E. A. Mittendorf, S. L. Moulder, W. F. Symmans, A. M. Thompson, H. Piwnica-Worms, C. H. Chen, K. H. Khoo, and M. C. Hung, "Metformin Promotes Antitumor Immunity via Endoplasmic-Reticulum-Associated Degradation of PD-L1," Mol. Cell **71**(4), 606–620.e7 (2018).
8. A. Anantharaman, T. Friedlander, D. Lu, R. Krupa, G. Premasekharan, J. Hough, M. Edwards, R. Paz, K. Lindquist, R. Graf, A. Jendrisak, J. Louw, L. Dugan, S. Baird, Y. Wang, R. Dittamore, and P. L. Paris, "Programmed death-ligand 1 (PD-L1) characterization of circulating tumor cells (CTCs) in muscle invasive and metastatic bladder cancer patients," BMC Cancer **16**(1), 744 (2016).
9. E. M. Rom-Jurek, N. Kirchhammer, P. Ugocsai, O. Ortmann, A. K. Wege, and G. Brockhoff, "Regulation of Programmed Death Ligand 1 (PD-L1) Expression in Breast Cancer Cell Lines In Vitro and in Immunodeficient and Humanized Tumor Mice," Int. J. Mol. Sci. **19**(2), 563 (2018).
10. W. Zhang, Q. Li, M. Tang, H. Zhang, X. Sun, S. Zou, J. L. Jensen, T. G. Liou, and A. Zhou, "A multi-scale approach to study biochemical and biophysical aspects of resveratrol on diesel exhaust particle-human primary lung cell interaction," Sci. Rep. **9**(1), 18178 (2019).
11. H. Zhang, W. Zhang, L. Xiao, Y. Liu, T. A. Gilbertson, and A. Zhou, "Use of Surface-Enhanced Raman Scattering (SERS) Probes to Detect Fatty Acid Receptor Activity in a Microfluidic Device," Sensors (Basel) 19 (2019).
12. W. Zhang, F. Lin, Y. Liu, H. Zhang, T. A. Gilbertson, and A. Zhou, "Spatiotemporal dynamic monitoring of fatty acid–receptor interaction on single living cells by multiplexed Raman imaging," *Proceedings of the National Academy of Sciences*, 201916238 (2020).
13. J. Taylor, A. Huefner, L. Li, J. Wingfield, and S. Mahajan, "Nanoparticles and intracellular applications of surface-enhanced Raman spectroscopy," Analyst **141**(17), 5037–5055 (2016).
14. J. Kim, S. H. Nam, D. K. Lim, and Y. D. Suh, "SERS-based particle tracking and molecular imaging in live cells: toward the monitoring of intracellular dynamics," Nanoscale **11**(45), 21724–21727 (2019).
15. Y. Shen, L. Liang, S. Zhang, D. Huang, J. Zhang, S. Xu, C. Liang, and W. Xu, "Organelle-targeting surface-enhanced Raman scattering (SERS) nanosensors for subcellular pH sensing," Nanoscale **10**(4), 1622–1630 (2018).
16. A. Kapara, V. Brunton, D. Graham, and K. Faulds, "Investigation of cellular uptake mechanism of functionalised gold nanoparticles into breast cancer using SERS," Chem. Sci. **11**(22), 5819–5829 (2020).
17. J. Kneipp, H. Kneipp, M. McLaughlin, D. Brown, and K. Kneipp, "In vivo molecular probing of cellular compartments with gold nanoparticles and nanoaggregates," Nano Lett. **6**(10), 2225–2231 (2006).
18. A. Huefner, W. L. Kuan, R. A. Barker, and S. Mahajan, "Intracellular SERS nanoprobes for distinction of different neuronal cell types," Nano Lett. **13**(6), 2463–2470 (2013).
19. A. Huefner, W. L. Kuan, K. H. Muller, J. N. Skepper, R. A. Barker, and S. Mahajan, "Characterization and Visualization of Vesicles in the Endo-Lysosomal Pathway with Surface-Enhanced Raman Spectroscopy and Chemometrics," ACS Nano **10**(1), 307–316 (2016).
20. J. A. Webb, Y. C. Ou, S. Faley, E. P. Paul, J. P. Hittinger, C. C. Cutright, E. C. Lin, L. M. Bellan, and R. Bardhan, "Theranostic Gold Nanoantennas for Simultaneous Multiplexed Raman Imaging of Immunomarkers and Photothermal Therapy," ACS Omega **2**(7), 3583–3594 (2017).
21. E. G. Lobanova and S. V. Lobanov, "Efficient quantitative hyperspectral image unmixing method for large-scale Raman micro-spectroscopy data analysis," Anal. Chim. Acta **1050**, 32–43 (2019).
22. J. F. Hsu, P. Y. Hsieh, H. Y. Hsu, and S. Shigeto, "When cells divide: Label-free multimodal spectral imaging for exploratory molecular investigation of living cells during cytokinesis," Sci. Rep. **5**(1), 17541 (2015).

Biomedical Optics EXPRESS


23. S. K. Paidi, P. M. Diaz, S. Dadgar, S. V. Jenkins, C. M. Quick, R. J. Griffin, R. P. M. Dings, N. Rajaram, and I. Barman, "Label-Free Raman Spectroscopy Reveals Signatures of Radiation Resistance in the Tumor Microenvironment," Cancer Res. **79**(8), 2054–2064 (2019).
24. H. Izabella J., J. Martin, W. Karina, B. Thomas, W. P. Mathias, C.-M. Dana, and P. Juergen, "Lab-on-a-chip-surface enhanced raman scattering combined with the standard addition method: toward the quantification of nitroxoline in spiked human urine samples," Anal. Chem. **88**(18), 9173–9180 (2016).
25. J. E. L. Villa, C. Pasquini, and R. J. Poppi, "Surface-enhanced Raman spectroscopy and MCR-ALS for the selective sensing of urinary adenosine on filter paper," Talanta **187**, 99–105 (2018).
26. T. T. Chuong, A. Pallaoro, C. A. Chaves, Z. Li, J. Lee, M. Eisenstein, G. D. Stucky, M. Moskovits, and H. T. Soh, "Dual-reporter SERS-based biomolecular assay with reduced false-positive signals," Proc. Natl. Acad. Sci. U. S. A. **114**(34), 9056–9061 (2017).
27. L. Sinha, Y. Wang, C. Yang, A. Khan, J. G. Brankov, J. T. Liu, and K. M. Tichauer, "Quantification of the binding potential of cell-surface receptors in fresh excised specimens via dual-probe modeling of SERS nanoparticles," Sci. Rep. **5**(1), 8582 (2015).
28. J. Jaumot, R. Gargallo, A. de Juan, and R. Tauler, "A graphical user-friendly interface for MCR-ALS: a new tool for multivariate curve resolution in MATLAB," Chemom. Intell. Lab. Syst. **76**(1), 101–110 (2005).
29. A. de Juan and R. Tauler, "Multivariate Curve Resolution (MCR) from 2000: Progress in Concepts and Applications," Crit. Rev. Anal. Chem. **36**(3-4), 163–176 (2006).
30. J. Canny, "A Computational Approach to Edge Detection," IEEE Trans. Pattern Anal. Mach. Intell. **PAMI-8**(6), 679–698 (1986).
31. Y. Tang, Y. Shen, L. Huang, G. Lv, C. Lei, X. Fan, F. Lin, Y. Zhang, L. Wu, and Y. Yang, "In vitro cytotoxicity of gold nanorods in A549 cells," Environ. Toxicol. Pharmacol. **39**(2), 871–878 (2015).
32. M. Remzova, R. Zouzelka, T. Brzicova, K. Vrbova, D. Pinkas, P. Rossner, J. Topinka, and J. Rathousky, "Toxicity of TiO2, ZnO, and SiO2 Nanoparticles in Human Lung Cells: Safe-by-Design Development of Construction Materials," Nanomaterials (Basel) 9(7), 968 (2019).
33. Z. Krpetic, S. Saleemi, I. A. Prior, V. See, R. Qureshi, and M. Brust, "Negotiation of intracellular membrane barriers by TAT-modified gold nanoparticles," ACS Nano **5**(6), 5195–5201 (2011).
34. L. A. Stanciu, C. M. Bellettato, V. Laza-Stanca, A. J. Coyle, A. Papi, and S. L. Johnston, "Expression of Programmed Death–1 Ligand (PD-L) 1, PD-L2, B7-H3, and Inducible Costimulator Ligand on Human Respiratory Tract Epithelial Cells and Regulation by Respiratory Syncytial Virus and Type 1 and 2 Cytokines," J. Infect. Dis. **193**(3), 404–412 (2006).
35. J. P. Smith, F. C. Smith, and K. S. Booksh, "Multivariate Curve Resolution-Alternating Least Squares (MCR-ALS) with Raman Imaging Applied to Lunar Meteorites," Appl. Spectrosc. **72**(3), 404–419 (2018).
36. L. A. Stanciu, C. M. Bellettato, V. Laza-Stanca, A. J. Coyle, A. Papi, and S. L. Johnston, "Expression of programmed death-1 ligand (PD-L) 1, PD-L2, B7-H3, and inducible costimulator ligand on human respiratory tract epithelial cells and regulation by respiratory syncytial virus and type 1 and 2 cytokines," J. Infect. Dis. **193**(3), 404–412 (2006).
37. J. Xue, L. Li, N. Li, F. Li, X. Qin, T. Li, and M. Liu, "Metformin suppresses cancer cell growth in endometrial carcinoma by inhibiting PD-L1," Eur. J. Pharmacol. **859**, 172541 (2019).
38. J.-J. Zhang, Q.-S. Zhang, Z.-Q. Li, J.-W. Zhou, and J. Du, "Metformin attenuates PD-L1 expression through activating Hippo signaling pathway in colorectal cancer cells," Eur. J. Pharmacol. **11**, 6965–6976 (2019).